Preprint Title	Computational Design for Enantioselective CO2 Capture: Asymmetric Frustrated Lewis Pairs in Epoxide Transformations
Authors	Maxime Ferrer, Iñigo Iribarren, Tim Renningholtz, Ibon Alkorta and Cristina Trujillo
Publication Date	09 Juli 2024
Article Type	Full Research Paper
Supporting Information File 1	beilstein-SI.pdf; 3.1 MB
ORCID® iDs	Iñigo Iribarren - https://orcid.org/0000-0003-0373-8687; Tim Renningholtz - https://orcid.org/0000-0001-8793-4057; Ibon Alkorta - https://orcid.org/0000-0001-6876-6211; Cristina Trujillo - https://orcid.org/0000-0001-9178-5146

Computational Design for Enantioselective CO_2 Capture: Asymmetric Frustrated Lewis Pairs in Epoxide Transformations

Maxime Ferrer*[1], Iñigo Iribarren[2], Tim Renningholtz[3], Ibon Alkorta[1] and Cristina Trujillo*[3,4]

Address: [1]Instituto de Química Médica (CSIC), Juan de la Cierva, 3, 28006 Madrid, Spain; [2]Technische Universität München (TUM), School of Computation, Information and Technology, Technische Universität München, D-85748 Garching bei München, Germany; [3]Department of Chemistry, The University of Manchester, Oxford Road, Manchester, M13 9PL, UK and [4]Trinity Biomedical Sciences Institute, School of Chemistry, The University of Dublin, Trinity College, D02 R590 Dublin 2, Ireland

Email: Maxime Ferrer - maxime.ferrer@iqm.csic.es; Cristina Trujillo - cristina.trujillodelvalle@manchester.a

* Corresponding author

Abstract

Carbon Capture and Utilisation (CCU) technologies offer a compelling strategy to mitigate rising atmospheric carbon dioxide levels. Despite extensive research on the CO_2 insertion into epoxides to form cyclic carbonates, the stereochemical implications of this reaction have been largely overlooked, despite the prevalence of racemic epoxide solutions. This study introduces an *in silico* approach to design asymmetric frustrated Lewis pairs (FLPs) aimed at controlling reaction stereochemistry. Four FLP scaffolds, incorporating diverse Lewis acids (LA), Lewis bases (LB), and substituents, were assessed via volcano plot analysis to identify the most promising catalysts. By strategically modifying LB substituents to induce asymmetry, a stereoselective catalytic scaffold was developed, favouring one enantiomer from both epoxide enantiomers. This work advances the *in silico* design of FLPs, highlighting their potential as asymmetric CCU catalysts with implications for optimising catalyst efficiency and selectivity in sustainable chemistry applications.

Keywords

FLP, asymmetric catalysis, CO_2, epoxy, volcano plot

Introduction

The field of frustrated Lewis pairs (FLP) has flourished since their seminal discovery in 2006 by Stephan *et al*.[1] These compounds, which feature a Lewis acid (LA) and a Lewis base (LB), whose interaction is hindered by bulky substituents or chain strain, have garnered significant attention. Initially explored for their ability to trap small molecules such as H_2, [2] CO_2, [3-5] N_2O, [6,7] and alkenes, [8,9] they have since found applications in catalysis. [10,11]

Among the first catalytic uses of FLPs was the hydrogenation of unsaturated compounds [10,12] and the reduction of CO_2 using H_2 as a reductant. [13] FLPs have become an attractive avenue for the reduction of CO_2, particularly given the increasing levels of CO_2 in the atmosphere. However, challenges persist in understanding and optimising the reactivity of these systems.

One significant obstacle is the tendency for CO_2 to react preferentially with FLPs over H_2. As such, the design of FLPs that prioritise the capture of H_2 over CO_2 becomes crucial for effective CO_2 reduction. [13] Additionally, the strength of the interaction between the catalyst and the resulting system after hydride transfer presents a limitation. The formation of a robust LA-oxygen interaction may impede proton transfer to the basic oxygen atom. These limitations suggest that a more viable approach to employing FLPs as catalysts for CO_2-related reactions could involve their use in CO_2 activation. [13] In particular, the capture of CO_2 by FLPs enhances the electrophilicity of the CO_2 carbon atom and the nucleophilicity of one of the CO_2 oxygen atoms. [4,13]

Carbon capture and utilisation (CCU) technologies involve the extraction of CO_2 from the atmosphere of the Earth to generate value-added chemicals, which can serve as platform chemicals in other chemical processes. [14,15] This is achieved by inserting CO_2 as a C1 building block into readily available substrates such as epoxides, resulting in the formation of polycarbonates or

monomeric cyclic carbonates. [16] Depending on the substitution pattern in the epoxide, a chiral centre is present in the product.

The insertion of CO_2 into epoxides has been the subject of numerous studies, but the stereochemical aspects of this reaction, particularly through the use of Frustrated Lewis Pair (FLP) catalysts, have been largely overlooked, despite the prevalence of racemic epoxide solutions. Only one study has addressed the asymmetric insertion of CO_2 into propylene oxide using a transition-metal catalyst. [17-19] Therefore, the stereochemical aspects of CO_2 insertion into propylene oxide enabled by FLP catalysts should be investigated.

To the best of our knowledge, only one paper has proposed an asymmetric approach to this reaction using a metal-based catalyst. [17] However, our approach differs significantly and seeks to explore new possibilities in this area.

Herein, the present study focusses on the asymmetric insertion of CO_2 into propylene oxide (PO) using asymmetric FLPs as catalysts. Initially, five FLP scaffolds with different substituents, LA and LB, were tested, resulting in a total of 53 potential catalysts (Scheme 1). The most promising catalyst scaffolds for the reaction under study were identified by volcano plot analysis (Scheme 1). [20,21] Inspired by the asymmetric oxazoline synthesised by Bochao *et al.*, [22] and guided by the volcano plot results, modifications to these FLP scaffolds facilitated the development of an asymmetric FLP and consequently an asymmetric catalyst. The subsequent study explores the asymmetric insertion of CO_2 into chiral PO catalysed by the proposed *in silico* designed catalyst.

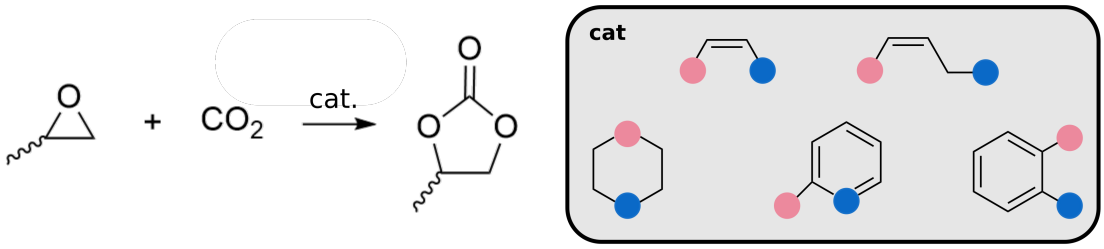

Scheme 1: Reaction between propylene oxide (PO) and CO_2 and the five catalyst scaffolds under study.

Computational Details

During the benchmark to choose the best catalyst, the reported geometries were optimised with the Gaussian16 quantum chemical software package, [23] using the B3LYP density functional [24,25] along with the Grimme dispersion correction including Becke and Johnson damping D3(BJ) [26-28] and the def2-TZVP basis set. [29] Harmonic frequencies were computed at the optimisation level to confirm that the relaxed structures correspond to local minima (no imaginary frequencies) or transition states (one imaginary frequency). The reaction simulations were run in chloroform using the Solvation Model based on Density (SMD) [30] at 273.0K to reproduce the most commonly used experimental conditions. [31-33]

When considering asymmetry, it was necessary to include large substituents on the catalyst to induce steric hindrance. These modifications, increase the size of the asymmetric catalysts. Thus, the calculations presented in the "Asymmetric catalysis" subsection were optimised at the B3LYP-D3(BJ)/def2-SVP computational level. Single point energy calculations on the optimised structures were run at the B3LYP-D3(BJ)/def2-TZVP to obtain more accurate electronic energies. The reported free energies in this section correspond to the sum of the triple-zeta electronic energy and the free energy correction at double-zeta.

The kinetics of some reactions were calculated, applying the transition state theory. [34] Within this theory, the rate constant of an elementary reaction with the free energy barrier $\Delta G^{\ddagger}$ is given by eq. (1)

$$k = \frac{k_b T}{h} e^{\frac{-\Delta G^{\ddagger}}{RT}} \tag{1}$$

where is the rate constant in s^{-1}, k_b is the Boltzmann constant, T is the temperature in Kelvin, h is the Planck constant, R is the gas constant.

The enantiomeric excess (%ee) was calculated using eq. (2). [35] k_{fav} stands for the kinetic rate

constant of the most favourable process, and k_{defav} stands for the rate constant of the less favourable process.

$$\%ee = \frac{k_{fav} - k_{defav}}{k_{fav} + k_{defav}} \tag{2}$$

During the asymmetric study, it will be observed that several TSs can lead to the same product. As there is no possible interconversion between the reactant states, the different reactions will be considered independent and it will be necessary to use an effective rate constant (k_{eff}). The definition given by Williams will be used (eq. (3), [36]).

$$k_{eff} = \sum_{j}^{N_{TS}} e^{-\Delta^{\ddagger} G_j / RT} \tag{3}$$

Volcanic 1.3.3, a Python package for the NaviCat platform, was used to generate 3D volcano plots, facilitating the identification of the most appropriate catalyst for the coupling reaction being considered. [21]

Volcano Plots

Volcano plots are a visualisation of the Sabatier principle, [37] a qualitative concept originating in heterogeneous catalysis for assessing the performance of different catalysts. According to this principle, an ideal catalyst interacts with reactants neither strongly nor weakly. This idea is visualised in volcano plots, where a metric of the catalyst performance, e.g. the reaction rate, is displayed as a function of the catalyst-substrate interaction, e.g. the adsorption energy when considering a heterogeneous catalyst (see Figure 1 (A)). The resulting plot exhibits a volcano-like shape consisting of at least two slopes with the best-performing catalysts located at the top. The top of the volcano plot corresponds to the scenario where the catalyst exhibits high catalytic activity, as it achieves an optimal balance in binding to the reactants, neither too strongly nor too weakly (see Figure 1

(A), purple points). The catalysts with binding energies lower than the catalysts at the top show lower catalytic activity due to insufficient activation of the substrate (see Figure 1 (A), green points). Conversely, catalysts that bind too strongly impede the detachment of the catalyst-reactant complex, thereby reducing the catalyst turnover (see Figure 1 (A), pink points). [20,21]

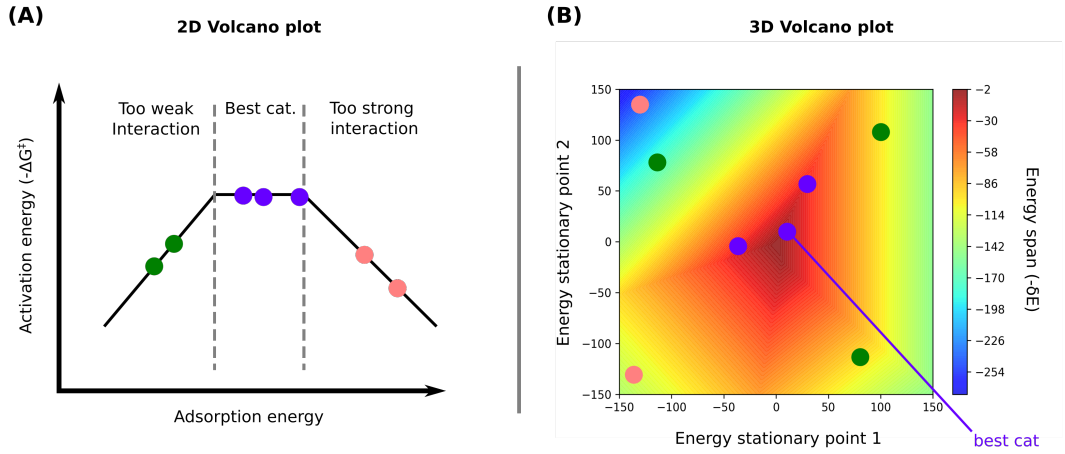

Figure 1: Schematic representation of a 2D (A) and 3D (B) volcano plot. "cat." stands for catalyst.

The previous plots are effective for metal-based catalysts and relatively simple catalytic reactions; however, they fall short when reactions involve multiple steps and independent activation barriers. In this paper, instead of focusing solely on activation energy, the energy span of the catalytic reaction (δE) is considered. King et al. [38] introduced the concept of the energy span of a simulated catalytic cycle by defining it as the difference between the highest and lowest free energy stationary points. [39,40] More precisely, the energy span can be defined using eq. (4), where T_i is the energy of the rate-limiting TS, I_j the energy of the most populated intermediate and $\delta G_{i,j}$ a correction that accounts for the cyclic nature of the catalytic cycle. [20]

$$\delta E = max_{i,j}(T_i - I_j) + \delta G_{i,j} \tag{4}$$

The energy span is a crucial parameter, as it directly correlates with the Turnover Frequency

(TOF) of the catalytic reaction (see Equation 5). A flatter energy profile, indicated by a δE closer to zero, signifies more efficient catalysis.

$$TOF = \frac{k_B T}{h} e^{\frac{-\delta E}{RT}} \tag{5}$$

In this work, to achieve better correlations between the energy span and the system energies, two energies were used (see Figure 1 (B)). The volcanic program employs a multivariate linear regression process. Considering a reaction with six stationary points (REACTANTS, E1, TS2, E2, TS3, PRODUCTS) and which can be catalysed by n potential catalysts, the program calculates the correlation between the energy span and all the possible pairs of stationary points for the n catalysts. For instance, it determines a function such as E1 = f(E2, TS3). The quality of these correlations is assessed through the square of the Pearson coefficient. The pair of stationary has to correlate with the energies of the six stationary point previously presented. The quality of the pair considered to describe well the energies of the catalytic reaction is thus obtained by taking the mean value of R^2 of the six correlations. The pair with the largest mean R^2, is considered as the optimal pair of stationary points, and it is then used to predict the energy span, resulting in a 2D contour plot (see Figure 1 (B)). The x-axis represents the free energy of the first stationary point of the selected pair and the y-axis represents the free energy of the other stationary point of the pair. According to the volcano plots, the best theoretically-predicted catalysts are those nearest to the lowest predicted δE values, depicted by the purple points in Figure 1 (B).

Results and Discussion

The following nomenclature will be used during the volcano plot analysis: FX_LBLA_S1_S2 where X is the label of the family (1, 2, 3, 5 or 6), LB the Lewis base considered (N or P), LA the Lewis acid (in this particular study only B), S1 the substituent on the LB, and S2 the substituent on the LA.

Capture of CO_2 and PO by an FLP

Chemoselectivity

Our investigations began by examining the uncatalysed coupling reaction between CO_2 and PO (Scheme 1), which exhibits a calculated activation barrier ($\Delta G^{\ddagger}$) greater than 55 kcal/mol. Therefore, in order to observe the coupling between these two moieties under standard conditions, the presence of a catalyst is necessary. In the literature, metal-based and organocatalysts have been reported as efficient catalysts for this reaction [18,19]. As noted previously [41,42], the reaction depicted in Scheme 1 can proceed via two distinct mechanisms.

In the first mechanism, the catalyst initiates epoxide opening, followed by CO_2 insertion. The second mechanism suggests that CO_2 activation by the catalyst precedes its transfer to the epoxide. To determine the more feasible mechanism, a comprehensive investigation of both possibilities was conducted.

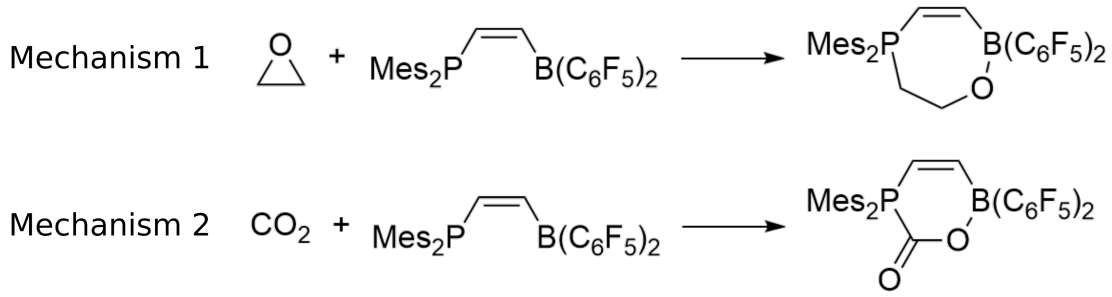

Scheme 2: Capture reactions of CO_2 or an epoxide by FLP

To determine the most probable mechanism within our system, the capture of CO_2 and a symmetric epoxide (E) using the FLP proposed by Stephan et al. [31] was evaluated (see Scheme 2). A symmetric epoxide was chosen to avoid addressing asymmetry concerns at this stage. The capture exhibiting the lowest activation barrier was considered the first step of the coupling reaction for the remainder of the study. The free-energy profiles of both capture processes are depicted in Figure S1. Notably, the CO_2 capture exhibits a lower activation barrier compared to the capture of epoxide (+10.0 kcalmol^{-1} *vs* +30.0 kcal/mol). Using transition state theory [34] as expressed in eq. (1), the rate constants were calculated for binding to either molecule at 273.0 K, resulting in k_1=5.47E+04 s^{-1} for

capturing CO_2 and k_2=4.85E-12 s^{-1} for capturing the epoxide. Despite the FLP-CO_2 adduct being less thermodynamically stable than the FLP-epoxide adduct (-10.1 kcal/mol *vs* -44.8 kcal/mol), the lower activation barrier for the capture of CO_2 and the temperature considered (273.0 K) suggest a kinetically controlled reaction. To further shift the chemical equilibrium toward CO_2 capture, increasing steric hindrance at the epoxide was explored by introducing bulky substituents into the scaffold. This resulted in an increase in activation barriers for adduct formation. Including a methyl group, for instance, increased the barrier by 1.4 kcal/mol, a phenyl group by 1.7 kcal/mol, and a tert-butyl group by more than 2 kcal/mol (Table S1). This observation is consistent with reports in the literature. [43-47]

Based on this initial study, it can be concluded that the mechanism for our system proceeds according to mechanism two. The following simulations were performed on this conclusion.

Regioselectivity

Propylene oxide (PO) exhibits two distinct electrophilic sites which can be subject to nucleophilic attack (Figure 2 (B)). Thus, the regioselectivity of the CO_2 insertion into PO must be addressed as part of the full mechanistic investigation. The 3-Boryl-2-propen-1-amine is now considered as the catalyst (Figure 2 (B)). As observed in Figure 2 (A), the bond length and electron density at the Bond Critical Point (BCP) difference are minimal and do not conclusively suggest that one bond will be broken more easily than the other. Therefore, both scenarios will be explored to see if the coupling reaction could proceed more easily by breaking the O-CH(CH_3) bond rather than the O-CH_2 bond.

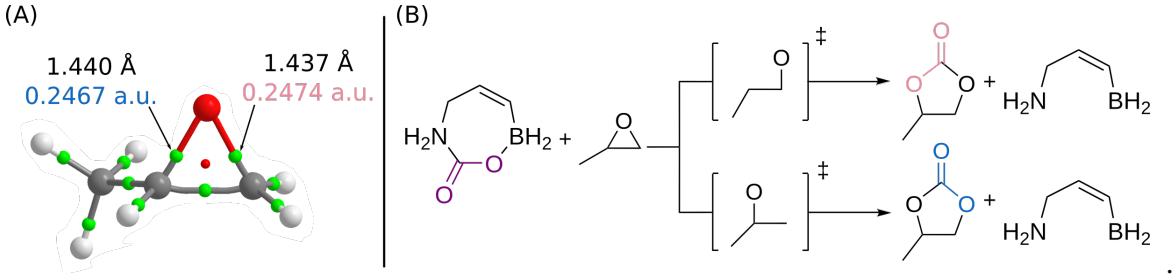

Figure 2: (A) Structure of PO annotated with the C-O bond distances and electron densities at the BCPs. BCPs are indicated by green spheres and the ring critical point by a red sphere. (B) Schematic representation of the two possible ring-opening of PO in the presence of activated CO_2

Based on our investigations, the opening of PO with activated CO_2 was found to proceed through two transition states. The calculations showed that the breaking of the O-CH(CH_3) bond was more kinetically favourable, with a TS 7.6 kcal/mol lower in free energy than the corresponding TS for breaking the O-CH_2 bond. The electron-donating nature of the methyl group facilitates a greater stabilisation of the intermediary positive charge at the central carbon compared to the hydrogen after bond-breaking at the terminal carbon, thereby reducing the activation barrier.

Henceforth, in this paper, the optimised TSs will consistently represent the breaking of the O-CH(CH_3) bond. Additionally, the *(S)*-epoxide enantiomer was employed consistently.

Symmetric FLP scaffolds - Achiral Environment

Following the initial exploration and preliminary results, our attention shifted toward the identification of a suitable catalyst. Drawing inspiration from the literature, fourteen FLP scaffolds have been evaluated (see Figure 3), focussing specifically on N/B and P/B FLPs due to their widespread application in this field, especially considering the initial step involving CO_2 capture. [4,10,15]

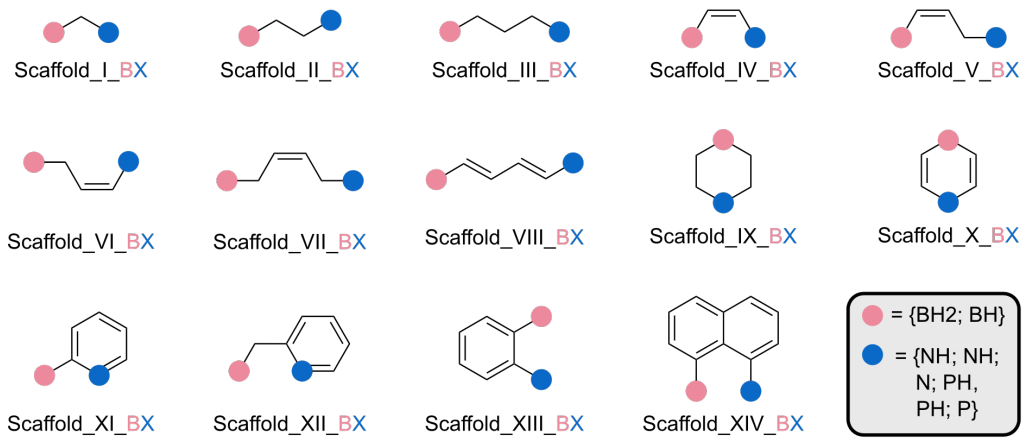

Figure 3: Symmetric FLP scaffolds considered in the first study. X denotes N or P.

Selection of the scaffolds and substituents

Volcano plots were introduced to find the most efficient catalyst for a given reaction. [20,48] They are a valuable tool for the *in silico* design of catalysts. [21,49] Volcano plot analysis requires a set of reactions that follow the same mechanism but whose stationary points possess different energies.

Generally, the larger the differences in energy between the stationary points, the better the exploration of the catalytic space.

To determine the set of scaffolds to be used for volcano plot analysis, the CO_2-FLP adduct of each of the fourteen scaffolds was optimised (see Figure 3). Based on the stability of the optimised adducts, families can be selected to cover a wide energy range. The obtained free energies of formation are presented in Figure S2. The stabilities of the N/B adducts range from -9 to +48 kcal/mol, while the P/B adducts vary from +10 to +36 kcal/mol. Due to the larger variation in the energy of the CO_2-FLP adduct employing N/B FLP, it was decided to choose the systems based on the FLPs with N/B. The scaffolds V_BX (family 1, ΔG(adduct)=-0.4 kcal.mol^{-1}), IX_BX (family 2, ΔG(adduct)=-2.1 kcal.mol^{-1}), XIII_BX (family 3, ΔG(adduct)=+3.0 kcal.mol^{-1}), IV_BX (family 4, ΔG(adduct)=+15.4 kcal.mol^{-1}) and XI_BX (family 5, ΔG(adduct)=-19.5 kcal.mol^{-1}) were selected for further investigation (Figure 4). This selection enables to obtaining a free energy differences of 35 kcal.mol^{-1} already in the adduct stationary point.

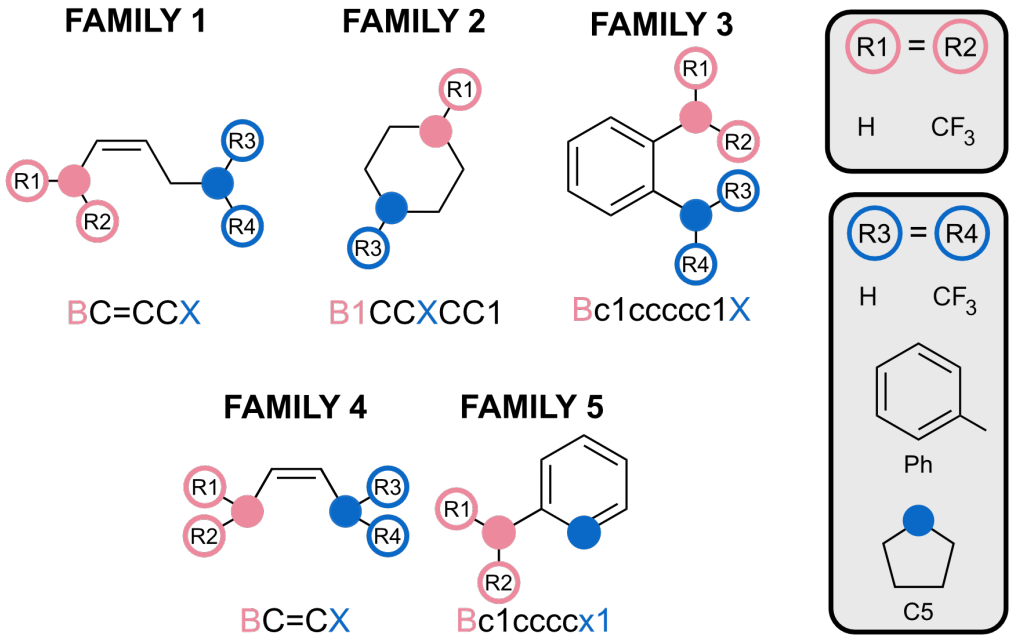

Figure 4: Subset of FLP scaffolds considered in the catalyst optimisation study. Substituents and labels are indicated.

After selecting the scaffolds to work with, the next step is to choose substituents for placement on the LA and LB positions. These substituents will have two main effects on the FLP: first, they

will alter the Lewis acidity and basicity of the LA and LB centres respectively; second, they may induce steric hindrance. The first effect is perhaps the most intriguing to consider, as the acidity and basicity of the LA/LB centres are indicative of the FLP's reactivity.[50,51] Thus, substituents must be selected to ensure a broad spectrum of acidity and basicity of the LA and LB. Different methods for determining these properties have been described in the literature. Due to their easy computation, the proton affinity [52] and fluoride ion affinity [53] were selected to compute the basicity and acidity of the systems considered. By selecting the substituents presented in Figure 4, it was observed that FIAs spanning a range of 60 kcal.mol^{-1} and PAs spanning a range of 48 kcal.mol^{-1} were obtained (Figure S3).

Possible mechanisms

As established in the previous section. the general mechanism of the coupling reaction proceeds through three steps: 1) capture of CO_2, 2) opening of PO and addition of the activated CO_2, 3) liberation of the product (Figure 5).

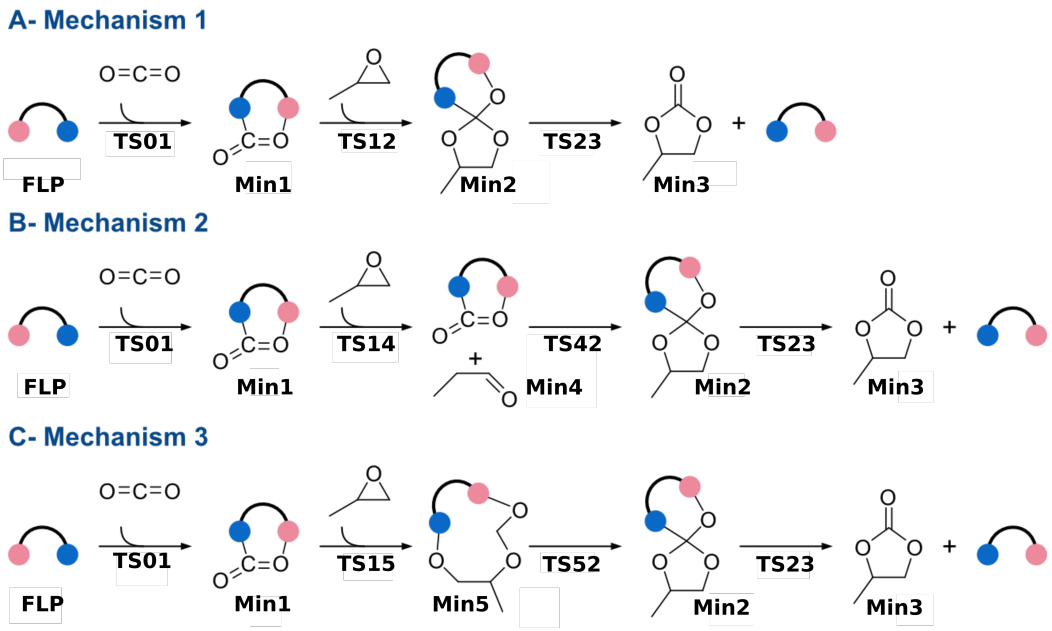

Figure 5: Coupling reaction between PO and CO_2. Depending on the catalyst considered, the reaction follows mechanisms 1, 2 or 3.

During the study of the selected catalysts (Figure 4), it was observed that depending on the

catalyst considered, the reaction followed a different mechanism: Mechanism 1, 2 or 3 (Figure 5). The mechanism 1 (Figure 5 (A)), comprises three steps. First, CO_2 is captured by FLP (TS01), and subsequently activated CO_2 is inserted into epoxy (TS12). TS12 corresponds to the concerted opening of PO and the insertion of CO_2. The product is later released via TS23. This mechanism is followed by 40% of the catalysed reactions studied. Mechanism 2 (Figure 5 (B)) contains an additional step. In this mechanism, the epoxy is first isomerised through TS14, resulting in the formation of the aldehyde (Min4). It can be observed that the opening of the epoxy is catalysed by the presence of the CO_2 adduct. In the gas phase and isolated, the isomerisation of the epoxy presents a barrier of 52.6 kcal.mol^{-1}. In the case of F2_NB_H_H, the barrier is reduced to 37.0 kcal.mol^{-1}. CO_2 later reacts with the aldehyde, forming the insertion product already observed in Mechanism 1 (Min2). Passing through TS23, the product is released. Similar to Mechanism 2, Mechanism 3 contains eleven stationary points (Figure 5 (C)). After the capture of CO_2 by the FLP, the opening of the epoxy takes place along with the insertion reaction. The main difference from the previous two mechanisms is that a new intermediate (Min5) is stabilised, in which the oxygen of CO_2 has attacked the electrophilic carbon of PO, and the oxygen atom of PO interacts with LB. This mechanism is exclusive to phosphorus-containing FLPs, as nitrogen does not support this type of reactivity. Subsequently, the intermediate undergoes reorganization, leading to Min2.

Surprisingly, family 5, having phosphorus as the Lewis base, presents different reactivity from the other families (Figure S3). Compounds F5_PB_H and F5_PB_CF3 react following Mechanism 3 (Figure 5 (C)), but the reaction proceeds directly from Min5 to Min3, with no Min2 observed. These two cases were then removed from the volcano plot analysis. The remaining two catalysts from family 5, namely F5_PB_H and F5_PB_H, react according to Mechanism 1 (Figure 5 (A), Figure S4). The energy matrix obtained can be found in Tables S2 and S3. It is interesting to observe that of the remaining 47 catalysts, 12 are not catalytically active, having their largest activation barrier greater than the 55.0 kcal.mol^{-1} previously reported for the uncatalysed reaction. Most of these belong to family 1.

Optimising Catalyst Selection

The optimal scaffolds and substituents for the studied reaction were identified through analysis using a volcano plot.This analysis requires that all catalytic cycles present the same number steps. Due to varying steps between mechanisms A, and B and C, they had to be treated separately. The first group comprises catalysts that produce reactions following mechanism 1 (Figure 5 (A)), characterised by nine stationary points. The second group consists of reactions with eleven stationary points, indicating that FLPs catalyse reactions following mechanisms 2 or 3 (Figure 5 (B) and (C)). For each group, an analysis was performed using two volcano plots. The first plot aids in identifying the best families, which are then exclusively considered for the second volcano plot. The second plot helps determine the most appropriate substituents to consider, thereby highlighting the optimal catalyst.

The first group of reactions, those following mechanism 1 (see Figure 5 (A)), comprises a total of twenty-two FLPs, accounting for 40% of the 55 catalysts considered. This group 1 includes FLPs from families 1, 3, 4 and 5. Sixteen compounds are based on an N/B pair, while the remaining six are P/B FLPs. Given the relative complexity of the mechanism studied, it was necessary to employ a 3D volcano plot using the energy span (δE) and two energies of the system. Analysis of the correlations revealed that the most suitable combination of energies to consider involved the energy of pre-TS01 assembly (PTS01) and the energy of the intermediate P3 (Figure 5). Correlating these parameters with the energy span yields an R^2 value of 0.79, a mean absolute error (MAE) of 2.59, and a standard mean absolute percentage error (MAPE) of 0.35.

As depicted in Figure 6(A), families 3, 4 and 5 emerge as catalysts that catalyse the reaction the most effectively. This aligns with previous findings that family 1 is not suitable for catalysing the reaction. However, it is noteworthy that compounds F1_PB_Ph_H, F1_PB_Ph_CF3 from family 1, are exceptions as they exhibit acceptable catalytic activity.

To identify the most suitable substituents, compounds of family 1 were excluded (except F1_PB_Ph_H, F1_PB_Ph_CF3) and a new volcano plot (see Figure 6 (B)) was generated. This plot employs the same axes as before ($\Delta G(PTS01), \Delta G(P3)$) and identifies a catalyst worthy of special consideration: F3_NB_C5_CF3.

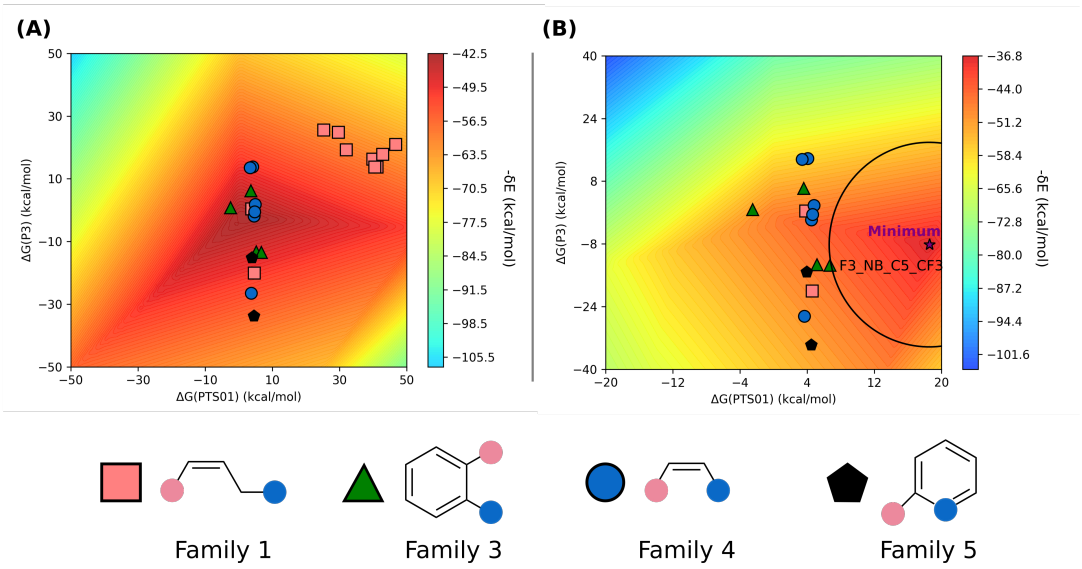

Figure 6: VOLCANO plot group 1. The free energies of PTS01 and P3 are considered for the correlation. On the left, the compounds of families 1, 3, 4 and 5 were used for the plot. On the right, only families 3, 4 and 5 are considered along with compounds F1_PB_Ph_H and F1_PB_Ph_CF3. In (B) A purple star was used to locate the minimum of the surface, along with a circle centre in the minimum to locate the closest systems. In the right figure, the names of the most effective catalysts are indicated in black.

Additionally, it is observed that an efficient catalyst for this reaction should have an unstable pre-TS assembly, PTS01, (E1 > 0) and an intermediate P3 with an energy close to 0 kcal/mol. Remarkably, among the most efficient catalysts within this group of FLPs those with a nitrogen LB stand out. This phenomenon could be attributed to the exceptional stability of the covalent adduct formed between phosphorus-based FLPs and CO_2.

The second group comprises compounds that undergo reactions following mechanisms 2 and 3 (Figure 5). This group represents 60% of the 55 catalysts considered. This time, the set is richer in FLPs based on phosphorus, comprising 21 out of 29 compounds. It includes compounds from families 1, 2, 3, and 4. Similarly to the previous group, a 3D volcano plot was utilised. The same variables (energy of PTS01 and P3) were considered, which yielded a correlation with a R^2 value of 0.71.

As depicted in Figure 7(A), it is clear that the best family for this mechanism is family 2, followed by families 3 and 4. Family 1, similar to the previous group, exhibits the lowest catalytic activity. The

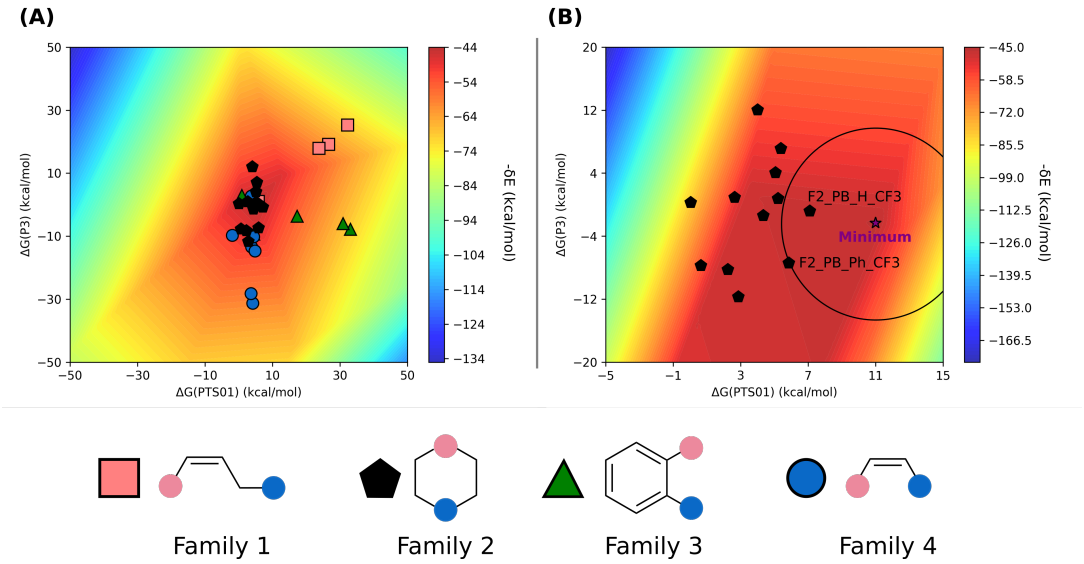

Figure 7: VOLCANO plot group 2. The free energies of pre-TS01 assembly and Min2 are considered for the correlation. On the left, the compounds of families 1, 2, 3 and 4 are depicted. On the right, only family 2 is considered. In (B) a purple star was used to locate the minimum of the surface, along with a circle centre in the minimum to locate the closest systems. In the right figure, the names of the most effective catalysts are indicated in black.

low reactivity could be attributed to the masked character of this family. FLP monomers belonging to family 1 can be considered as "masked-FLP", [54][55] requiring breaking the LA-LB bond to achieve reactivity. Consequently, the pre-TS assembly formed between CO_2 and the FLPs from family 1 are less stable than the pre-TS assembly between CO_2 and the other FLP families, due to the absence of possible interactions between CO_2 and Lewis acid (LA) or Lewis base (LB). Furthermore, TS01, corresponding to the capture of CO_2, is higher in energy due to the need for breaking the LA-LB bond.

By exclusively considering family 2 and using the energy of pre-TS01 assembly and the product P4 for the second volcano plot (see Figure 7(B)), it is observed that the best candidates are F2_PB_H_CF3 and F2_PB_Ph_CF3. Then it can be concluded that the catalytic activity of the FLP is more efficient if the boron bears CF_3 substituents. Thus, an acidic boron atom seems to increase the reactivity of the considered system. Concerning LB, it appears that, as opposed to the first group of compounds, a phosphorus atom is more active than a nitrogen atom.

Asymmetric catalysis

After examining the volcano results, we looked into the literature to explore examples of asymmetric frustrated Lewis pairs (FLPs). This exploration revealed three main types: intramolecular chiral FLPs, intermolecular FLPs composed of a chiral acid and an achiral base, and intermolecular FLPs comprising an achiral acid and a chiral base. [56,57] One study reported a reaction involving the asymmetric reduction of ketones using an achiral borane, denoted as $B(p-HC_6F_4)_3$, paired with a chiral oxazoline, as depicted in Scheme 3. [22] Remarkably, in this study, these FLPs demonstrated the capability to achieve high conversion rates and enantiomeric excess.

Following the volcano plot analysis presented in the previous section, F3_NB_C5_CF3 emerged as one of the top FLP catalysts under study. This catalyst, adhering to mechanism 1, incorporates a CF_3 group on the boron, serving as a simplified version of the $B(p-HC_6F_4)_3$ substituent. Notably, the nitrogen in this FLP is situated within a five-membered ring. Using this structural insight, an asymmetric catalyst was subsequently designed by strategically modifying the pyrrolidine substituent (C5 in Figure 4) based on the most efficient FLP.

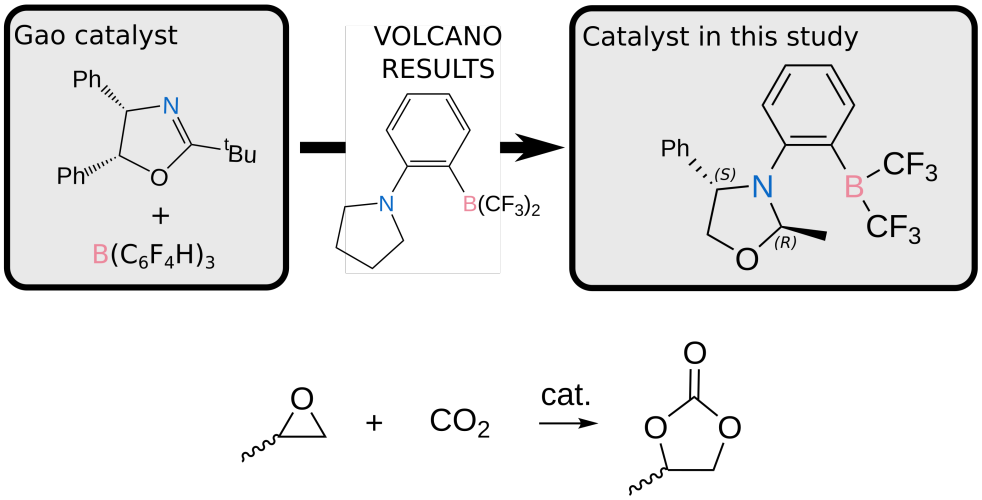

Scheme 3: Asymmetric catalysis studied. On the left the catalyst proposed by Gao *et al.* for the asymmetric hydrogenation of a ketone. [22] On the right the catalyst design inspired by the Gao catalyst and the volcano plot results. At the bottom, the reaction under study.

The coupling reaction proposed in Scheme 3 was studied. In order to minimise the computational costs associated with the study, the asymmetric catalyst was obtained by removing a phenyl group

and changing the ^{t}Bu group by a methyl group in the catalyst of Gao. [22] It appears that the capture of CO_2 by the catalyst is barrierless and results in the formation of an adduct with a relative free energy of 0.7 kcal.mol^{-1}. Thus, the evaluation of the stereoselectivity of the designed catalyst was conducted by only studying the steps after the capture of CO_2 by the catalyst.

Table 1: Free energy reaction profile of the asymmetric coupling between the propylene oxide and CO_2 catalysed by the catalyst depicted in Scheme 3. The energies are reported in kcal/mol and the 0.0 energy was set to be the FLP – CO_2 adduct and the propylene oxide isolated.

Enantiomer	Pre-TS	TS1	Int.	Asymmetric TS	Product
R	9.4	27.6	27.9	30.9	-14.2
S	8.9	25.0	24.5	32.1	-13.4

The reaction occurs in two steps (Table 1). Initially, a pre-TS assembly, with the PO compound positioned 2.67 Å from the CO_2 carbon is formed. Overcoming a transition state (TS) an intermediate is generated. In this intermediate, the distance between PO and the CO_2 carbon decreases to 1.61Å from the initial 2.67Å, and the interaction between nitrogen and the CO_2 carbon weakens. The intermediate is highly energetic and closely positioned to the transition state (TS). In the case of the (*R*)-mechanism, the intermediate is slightly higher in energy than the TS, potentially due to methodological error. The intermediate further reacts with the activated CO_2 to generate the corresponding product. As can be observed in Table 1, the mechanism leading to the (S)-product presents an asymmetric TS 1.2 kcal.mol^{-1} higher in energy than the (R)-mechanism. Thus, the asymmetric catalyst enables to generate an enantiomeric excess of 95%, the (R)-product being the most abundant product.

Surprisingly, a transition state connecting the (S)-epoxy with the (R)-product was identified (Figure 8). Even more intriguingly, this new TS (TS_S_R in), verified by the IRC calculation (Figure S5) is the most stable TS located (Figure 9).

In this TS, the epoxy ring opens (Figure 9). Due to a shorter C-C distance between the CH_3 group in the catalyst and the epoxy carbon (3.45 Å vs 3.75 Å in TS_S_S), a steric clash between the two methyl groups occurs (Figure 9). This results in an inversion of stereochemistry via rotation of the epoxy C-C bond, leading to the formation of the (*R*)-product. As two TSs now yield the same product, it is necessary to recalculate the $\%ee$, but this time using an effective rate constant k_{eff}

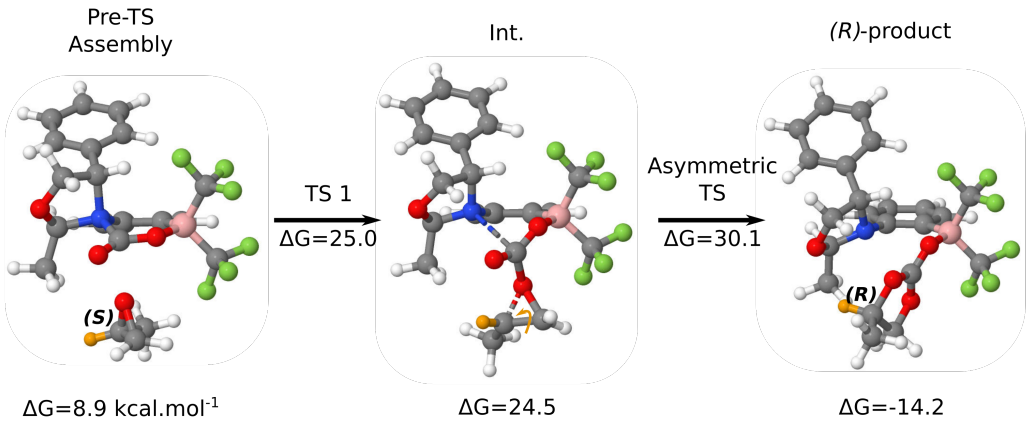

Figure 8: Catalysed reaction between the (S)-enantiomer of propylene oxide and CO_2 resulting in the formation of the (*R*)-product. In orange, the hydrogen atom that illustrates the stereochemistry inversion. The free energies are given in kcal.mol^{-1}

(eq. (3)). In doing so, a small increase in enantioselectivity is observed, with now, a (*R*) enantiomeric excess of 96 %. The designed catalyst enables the generation of an almost enantiomerically pure product from a racemic mixture.

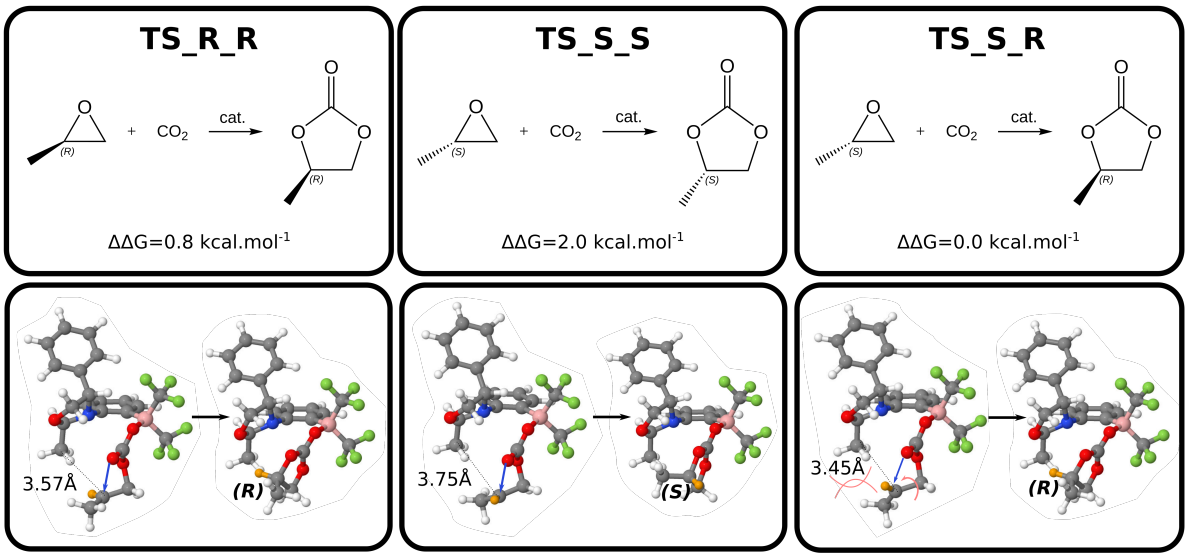

Figure 9: Scheme of the different asymmetric reactions observed. Hydrogen capable of rotation is marked in orange, influencing the stereochemistry at TS.

Conclusions

Carbon Capture and Utilisation (CCU) technologies represent a promising avenue for addressing increasing atmospheric carbon dioxide levels. The reaction involving the insertion of CO_2 into epoxides to form cyclic carbonates is a key focus within this domain. Despite extensive exploration, the stereochemical aspects of this reaction have been surprisingly underexplored, especially in the context of racemic epoxide mixtures commonly encountered in practice.

This study introduces an innovative *in silico* design strategy for asymmetric frustrated Lewis pairs (FLPs) tailored specifically to control the stereochemistry of the CO_2 insertion reaction. Computational evaluations of four distinct FLP scaffolds, incorporating various Lewis acids (LA), Lewis bases (LB), and substituents, identify the most promising catalyst candidates through volcano plot analysis.

Through strategic modification of the Lewis base substituents, a stereoselective catalyst was engineered to produce a single enantiomer preferentially from both enantiomers of the epoxide substrate. An enantiomeric excess of 95% was initially achieved, with the predominant (*R*)-enantiomer. Enhanced selectivity was subsequently observed through additional transition states, resulting in a remarkable 96% enantiomeric excess being achieved by the catalyst.

Supporting Information

Supporting information features geometries of the different stationary points optimised as well as figures and tables mentioned in the main text. The outputs of the calculations presented can be found at the following link: https://doi.org/10.5281/zenodo.12633864

Supporting Information File 1:

File Name: SI_Computational_Design_for_Enantioselective_CO2_Capture_Asymmetric_Frustrated_Lewis_Pairs_in_Epoxide_Transformations.pdf

File Format: PDF

Title: Supporting figures and tables

Acknowledgements

This publication has emanated from research supported by Science Foundation Ireland (SFI 18/SIRG/5517) and t he Ministerio de Ciencia, Innovación y Universidades (PID2021-125207NB-C3). For Open Access purposes, the author has applied a CC BY public copyright license to any Author Accepted Manuscript version arising from this submission. The authors acknowledge the assistance provided by Research IT and the use of the Computational Shared Facility at The University of Manchester, HPC-Europe3, the Centro de Supercomputacion de Galicia (CESGA), and the Irish Centre for High-End Computing (ICHEC) for their continued computational support. Additionally, the authors express their gratitude to Dr. Rubén LaPlaza for his valuable scientific discussions and insights.

Funding

SFI 18/SIRG/5517 and PID2021-125207NB-C3

References

1. Welch, G. C.; Juan, R. R. S.; Masuda, J. D.; Stephan, D. W. *Science* **2006**, *314*, 1124–1126.
2. Stephan, D. W. *J. Am. Chem. Soc.* **2021**, *143*, 20002–20014.
3. Stephan, D. W.; Erker, G. *Chem. Sci.* **2014**, *5*, 2625–2641.
4. Pérez-Jiménez, M.; Corona, H.; de la Cruz-Martínez, F.; Campos, J. *Chem. Eur. J.* **2023**, *29*, e202301428.
5. Khan, M. N.; van Ingen, Y.; Boruah, T.; McLauchlan, A.; Wirth, T.; Melen, R. L. *Chem. Sci.* **2023**, *14*, 13661–13695.
6. Otten, E.; Neu, R. C.; Stephan, D. W. *J. Am. Chem. Soc.* **2009**, *131*, 9918–9919.
7. Neu, R. C.; Otten, E.; Lough, A.; Stephan, D. W. *Chem. Sci.* **2011**, *2*, 170–176.
8. Ullrich, M.; Seto, K. S.-H.; Lough, A. J.; Stephan, D. W. *Chem. Commun.* **2009**, 2335–2337.

9. Jie, X.; Sun, Q.; Daniliuc, C. G.; Knitsch, R.; Hansen, M. R.; Eckert, H.; Kehr, G.; Erker, G. *Chem. Eur. J.* **2020**, *26*, 1269–1273.

10. Stephan, D. W. *Acc. Chem. Res.* **2015**, *48*, 306–316.

11. Paradies, J. *Eur. J. Org. Chem.* **2019**, *2019*, 283–294.

12. Scott, D. J.; Fuchter, M. J.; Ashley, A. E. *Chem. Soc. Rev.* **2017**, *46*, 5689–5700.

13. Khan, M. N.; van Ingen, Y.; Boruah, T.; McLauchlan, A.; Wirth, T.; Melen, R. L. *Chem. Sci.* **2023**, *14*, 13661–13695.

14. Song, Q.-W.; Zhou, Z.-H.; He, L.-N. *Green Chem.* **2017**, *19*, 3707–3728.

15. Fu, H.-C.; You, F.; Li, H.-R.; He, L.-N. *Front. Chem.* **2019**, *7*, 525.

16. Song, X.; Wang, J.; Yang, L.; Pan, H.; Zheng, B. *Inorg. Chem. Comm.* **2020**, *121*, 108197.

17. Berkessel, A.; Brandenburg, M. *Org. Lett.* **2006**, *8*, 4401–4404.

18. Andrea, K. A.; Kerton, F. M. *ACS Cat.* **2019**, *9*, 1799–1809.

19. Horton, T. A. R.; Wang, M.; Shaver, M. P. *Chem. Sci.* **2022**, *13*, 3845–3850.

20. Wodrich, M. D.; Sawatlon, B.; Busch, M.; Corminboeuf, C. *Acc. Chem. Res.* **2021**, *54*, 1107–1117.

21. Laplaza, R.; Das, S.; Wodrich, M. D.; Corminboeuf, C. *Nat. Protoc.* **2022**, *17*, 2550–2569.

22. Gao, B.; Feng, X.; Meng, W.; Du, H. *Angew. Chem. Int. Ed.* **2020**, *59*, 4498–4504.

23. Gaussian Inc. Wallingford CT

24. Becke, A. D. *J. Chem. Phys.* **1992**, *96*, 2155–2160.

25. Lee, C.; Yang, W.; Parr, R. G. *Phys. Rev. B* **1988**, *37*, 785–789.

26. Grimme, S.; Antony, J.; Ehrlich, S.; Krieg, H. *J. Chem. Phys.* **2010**, *132*, 154104.

425 27. Becke, A. D.; Johnson, E. R. *J. Chem. Phys.* **2005**, *123*, 154101.

426 28. Grimme, S.; Ehrlich, S.; Goerigk, L. *J. Comp. Chem.* **2011**, *32*, 1456–1465.

427 29. Weigend, F. *Phys. Chem. Chem. Phys.* **2006**, *8*, 1057–1065.

428 30. Marenich, A. V.; Cramer, C. J.; Truhlar, D. G. *J. Phys. Chem. B* **2009**, *113*, 6378–6396.

429 31. Mömming, C.; Otten, E.; Kehr, G.; Fröhlich, R.; Grimme, S.; Stephan, D.; Erker, G. *Angew.*
430 *Chem. Int. Ed.* **2009**, *48*, 6643–6646.

431 32. Krachko, T.; Nicolas, E.; Ehlers, A. W.; Nieger, M.; Slootweg, J. C. *Chem. Eur. J.* **2018**, *24*,
432 12669–12677.

433 33. Dalpozzo, R.; Della Ca', N.; Gabriele, B.; Mancuso, R. *Catalysts* **2019**, *9*, 511.

434 34. Eyring, H. *J. Chem. Phys.* **1935**, *3*, 107–115.

435 35. Schneebeli, S. T.; Hall, M. L.; Breslow, R.; Friesner, R. *JACS* **2009**, *131*, 3965–3973.

436 36. Williams, I. H. *J. Phys. Org. Chem.* **2022**, *35*, year.

437 37. Sabatier, P. *La catalyse en chimie organique*; C. Beanger, 1920; Vol. 3.

438 38. King, E. L.; Altman, C. *J. Phys. Chem.* **1956**, *60*, 1375–1378.

439 39. Kozuch, S.; Shaik, S. *JACS* **2006**, *128*, 3355–3365.

440 40. Kozuch, S.; Shaik, S. *Acc. Chem. Res.* **2011**, *44*, 101–110.

441 41. Fiorani, G.; Guo, W.; Kleij, A. W. *Green Chem.* **2015**, *17*, 1375–1389.

442 42. Shaikh, R. R.; Pornpraprom, S.; D'Elia, V. *ACS Cat.* **2018**, *8*, 419–450.

443 43. Kayaki, Y.; Yamamoto, M.; Ikariya, T. *Angew. Chem. Int. Ed.* **2009**, *48*, 4194–4197.

444 44. Maya, E. M.; Rangel-Rangel, E.; Díaz, U.; Iglesias, M. *Journal of CO2 Utilization* **2018**, *25*,
445 170–179.

45. Tsutsumi, Y.; Yamakawa, K.; Yoshida, M.; Ema, T.; Sakai, T. *Org. Lett.* **2010**, *12*, 5728–5731.

46. Chatelet, B.; Joucla, L.; Dutasta, J.-P.; Martinez, A.; Szeto, K. C.; Dufaud, V. *J. Am. Chem. Soc.* **2013**, *135*, 5348–5351.

47. Andrea, K. A.; Kerton, F. M. *ACS Cat.* **2019**, *9*, 1799–1809.

48. Stratton, S. M.; Zhang, S.; Montemore, M. M. *Surf. Sci. Rep.* **2023**, *78*, 100597.

49. Wodrich, M. D.; Busch, M.; Corminboeuf, C. *Chem. Sci.* **2016**, *7*, 5723–5735.

50. Ferrer, M.; Alkorta, I.; Elguero, J.; Oliva-Enrich, J. M. *ChemPhysChem* **2022**, *23*, e202200204.

51. Ferrer, M.; Alkorta, I.; Elguero, J.; Oliva-Enrich, J. M. *Phys. Chem. Chem. Phys.* **2024**, *26*, 12433–12443.

52. Kolboe, S. *J. Chem. Theo. Comp.* **2014**, *10*, 3123–3128.

53. Erdmann, P.; Leitner, J.; Schwarz, J.; Greb, L. *ChemPhysChem* **2020**, *21*, 987–994.

54. Fontaine, F.-G.; Stephan, D. W. *Philosophical Transactions of the Royal Society A: Mathematical, Physical and Engineering Sciences* **2017**, *375*, 20170004.

55. Ferrer, M.; Alkorta, I.; Elguero, J.; Oliva-Enrich, J. M. *ChemPhysChem* **2024**, *25*, e202300750.

56. Xiangqing Feng, W. M.; Du, H. Frustrated Lewis Pair Catalyzed Asymmetric Reactions. In *Frustrated Lewis Pairs*; Slootweg, J. C., Jupp, A. R., Eds.; Springer, 2021; pp 29–86.

57. Kótai, B.; Laczkó, G.; Hamza, A.; Pápai, I. *Chem. Eur. J.* **2024**.